Compact off-axis reflective optical system design combining freeform mirror and freeform detector

Jiawei Liu, Emmanuel Hugot, Eduard Muslimov, Simona Lombardo

Optics Communications 565 (2024) 130675

Contents lists available at ScienceDirect

Optics Communications

journal homepage: www.elsevier.com/locate/optcom

Compact off-axis reflective optical system design combining freeform mirror and freeform detector

Jiawei Liu [a,b,*], Emmanuel Hugot [a,b], Eduard Muslimov [a,c], Simona Lombardo [a]

[a] Aix Marseille Univ, CNRS, CNES, LAM, Marseille, France
[b] CURVE s.a.s./Curve-One, Marseille, France
[c] Department of Physics (Astrophysics), University of Oxford, Denys Wilkinson Building, Keble Road, Oxford, OX1 3RH, UK

ARTICLE INFO

Keywords:
Off-axis system
Compact design
Freeform mirror
Curved detector

ABSTRACT

Minimizing system size and weight without sacrificing the desired imaging performance is a crucial and challenging goal in the design of off-axis optical systems. In this paper, we propose a design concept that combines freeform mirror and freeform detector to achieve more compact off-axis optical systems. Initially, by applying nodal aberration theory, the optimal focal surface shape for off-axis systems is demonstrated to be an off-axis paraboloid or even a freeform surface, rather than the commonly assumed spherical shape. Subsequently, we show the ability of the design concept to reduce off-axis system volume through a design example of a fast and wide-field off-axis three-mirror system. Results indicate that, under the same design parameters and imaging quality, the design with a freeform detector is 80% smaller than that with a flat detector in terms of volume. Finally, the bending capability of the freeform detector presented in this paper is ensured through finite element analysis, and its surface accuracy is achievable based on the current precision level of curved detector fabrication. The proposed design concept holds promise for application in planetary science, where the imaging performance of the instrument is highly required and the size and weight are strictly limited.

1. Introduction

Off-axis reflective optical imaging systems offer numerous advantages, such as no chromatic aberration, no obscuration, high transmittance, and good thermal stability [1]. Therefore, they are applied in various fields including astronomical telescopes [2], spectrometers [3], optical remote sensing [4], and lithography [5]. However, the rotationally variant aberrations in off-axis systems cannot be effectively corrected by spherical or aspherical optical elements with rotational symmetry [6]. This has led to the design of off-axis systems being limited to narrow fields of view, large F-numbers, and often accompanied by large volumes [7]. Fortunately, the development of freeform optics has changed this scenario. By adding more degrees of freedom to optical mirror surfaces, the various rotationally variant aberrations present in off-axis systems are well corrected [8]. Thus, their application has greatly improved the field of view, F-number, and compactness of off-axis systems [9–11]. Nevertheless, freeform optics are not a universal solution for correcting all aberrations. Despite their substantial surface freedom, the correction of field curvature still relies on the traditional flat-field condition [6]. This condition necessitates that the sum of the optical powers of all mirrors be near zero to obtain a flat image plane compatible with commercial detectors. Consequently, flat-field condition somewhat constrains the parameter space reachable by freeform off-axis optical systems [12]. Bauer explored the minimum volume achievable by freeform off-axis three-mirror systems under different optical parameters [13]. While how to further break through the volume boundary of the current freeform off-axis systems is still a challenging problem.

In fact, the release of flat-field constraints can be achieved by using curved detectors, which can compensate for the field curvature aberration of optical systems directly at the focal plane position [14]. Therefore, their use can help simplify optical systems or improve system imaging performance. Over the past 15 years, several research institutions and companies, including Stanford [15,16], ESO [17,18], CEA-LETI [19,20], LAM [21,22], Sony [23], and Microsoft [24], have developed different methods to bend monolithic silicon to manufacture curved detectors. These curved detectors exhibit comparable photoelectric performance to flat detectors [25], and they find applications in astronomical telescopes [26,27], ultraviolet aurora monitoring [28], cerebral cortex imaging [29], and commercial lenses [30]. It is worth

* Corresponding author. Aix Marseille Univ, CNRS, CNES, LAM, Marseille, France.
E-mail address: liu.jiawei@lam.fr (J. Liu).

https://doi.org/10.1016/j.optcom.2024.130675
Received 17 January 2024; Received in revised form 12 April 2024; Accepted 4 May 2024
Available online 10 May 2024

noting that current research on curved detectors primarily focuses on spherical detectors, while overlooking the complexity of optical system focal surface. Specifically, when an optical system is tilted or decentered, the field curvature aberration no longer possesses rotational symmetry, and the aberration distribution becomes complex [31]. In such cases, spherical detectors cannot adequately compensate for such irregular field curvature aberration, and the residual field curvature aberration correction still requires optical elements to handle. Muslimov designed an off-axis three-mirror telescope using toroid detector [32,33], where only two cross-sections of the focal surface are considered, but no information is given about the exact shape of the entire focal surface in off-axis optical systems. It can be anticipated that if this irregular field curvature aberration can be adequately compensated for by a certain shape of curved detector, then the potential of freeform off-axis optical systems can be fully unleashed, thereby achieving smaller and lighter optical systems.

In this paper, we propose combining freeform mirror and freeform detector in the design of off-axis systems aiming to further reduce the system size and weight. The design concept leverages the complementary nature of the two technologies in terms of aberration correction, allowing the freeform detector to correct the irregular field curvature of off-axis systems, while the freeform mirror corrects other optical aberrations. In addition, in this study we pay special attention to applications in the field of planetary science, where the performance of imaging instruments is often highly demanding while their size and weight are strictly limited. In the beginning of the study, we analyze the optimal focal surface shape for off-axis systems through nodal aberration theory and mathematically prove that freeform detector can more adequately compensate for the irregular field curvature in off-axis systems. Subsequently, an off-axis three-mirror optical system design (12.4° diagonal field of view and fast aperture of F/2) is taken as an example to demonstrate the ability of the proposed design concept in reducing the size of off-axis optical systems. The design results are given by a comparative study between three designs based on flat, spherical and freeform image surfaces respectively. Furthermore, the manufacturability of the freeform detector is evaluated based on the mechanical limits of the material and the current precision level of detector curving technology to ensure its successful fabrication. Finally, we discuss the potential of the proposed design concept to extend the parameter space of optical imaging instruments in the field of planetary exploration.

The remainder of this paper is organized as follows. In Section 2, the theoretical analysis of the optimal focal surface shape for off-axis optical systems is presented. In Section 3, the optical design and simulation results of the off-axis three mirror optical system are detailed. In Section 4, the manufacturability of the freeform detector is evaluated. In Section 5, the application perspectives of the proposed design concept are discussed. Finally, a summary is given in Section 6.

2. Optimal focal surface shape for off-axis optical systems

In this section, the optimal focal surface shape for off-axis optical system is analyzed and illustrated. When optical system transitions from coaxial to off-axis, the traditional scalar aberration theory are no longer applicable. Instead, the vectorial nodal aberration theory is adopted here as a tool to analyze the best focal surface shape for off-axis optical imaging systems. Nodal aberration theory, discovered by Shack and developed by Thompson, describes the two-dimensional aberration field behavior of asymmetric optical system with rotationally symmetric components. In this theory, the field curvature aberration is described by medial focal surface rather than Petzval surface that commonly used with Seidel aberrations. It is the surface upon which the minimum RMS wavefront is measured. And the reference axis used in asymmetric systems called optical axis ray (OAR), which is defined as the ray that passes through the center of the image plane and the pupils for all the surfaces in the system. Additionally, the field point anywhere in the image plane is located by the vector $\vec{H}$, which starts from the intersection point of OAR with the Gaussian image plane. Similarly, the aperture point in the exit pupil can be located by the vector $\vec{\rho}$ and starts from the intersection point of OAR with the exit pupil plane.

From Thompson's work, we know that the wave aberration field of third order field curvature can be expressed by equation (1) [31]. Where W_{220M} represents the third-order wave aberration coefficient of field curvature measured at the medial focal surface. $\vec{H}_{220M}$ represents the effective field height vector originating from the vector $\vec{a}_{220M}$, so we have $\vec{H}_{220M} = \vec{H} - \vec{a}_{220M}$. Vector $\vec{a}_{220M}$ and scalar b_{220M} are normalized parameters associated with the tilt and decentration of each component $\vec{\sigma}_j$ in the system, specifically $\vec{a}_{220M} = \sum W_{220Mj}\vec{\sigma}_j / W_{220M}$, $b_{220M} = \sum W_{220Mj}\left(\vec{\sigma}_j \cdot \vec{\sigma}_j\right)/W_{220M} - \vec{a}_{220M}\cdot\vec{a}_{220M}$. It is found that the third order field curvature aberration field in asymmetric systems have one node that is out of the field center and located by $\vec{a}_{220M}$. When optical system is rotationally symmetric, $\vec{a}_{220M}$ and b_{220M} become zero, then $\vec{H}_{220M}$ is equal to $\vec{H}$, so the vector equation for field curvature wave aberration simplifies into the familiar scalar form $W_{220M}H^2\rho^2$.

$$W_{normalized\ third\ order\ field\ curvature} = W_{220M}\left[\left(\vec{H}_{220M}\cdot\vec{H}_{220M}\right) + b_{220M}\right](\vec{\rho}\cdot\vec{\rho}) \quad (1)$$

In addition, the third order plus fifth order field curvature wave aberration is also presented to show the influence of high order aberrations on field curvature aberration field. In equation (2) [34], W_{220ME} denotes the third-order wave aberration coefficient of field curvature affected by the fifth-order term W_{420M}, and $W_{220ME} = W_{220M} + 4W_{420M}b_{420M}$. Besides $\vec{H}_{220ME}$, $\vec{a}_{220ME}$ and b_{220ME} are the corresponding adjusted vectors, they are different from those used in the third-order wave aberration equation (1), and the vector $\vec{H}_{220ME}$ originates from the vector $\vec{a}_{220ME}$. Additionally, W_{420M} represents the fifth-order wave aberration coefficient of field curvature measured at the medial focal surface. $\vec{H}_{420M}$ is the effective field height vector originating from the vector $\vec{a}_{420M}$, so $\vec{H}_{420M} = \vec{H} - \vec{a}_{420M}$. $\vec{a}_{420M}$ and $\vec{b}_{420M}$ are normalized vectors in fifth order term and associated with the tilt and decentration of optical component $\vec{\sigma}_j$ in the off-axis system. From equation (2), three collinear zeros $\vec{a}_{420M}$ and $\vec{a}_{420M} \pm i\sqrt{2}\vec{b}_{420M}$ are found in the second term, which are the three nodes in fifth order field curvature aberration field. Similarly, in the rotationally symmetric system, the vector parameters that are related to system tilt and decenter become zero, equation (2) degenerates into the scalar form of $W_{220ME}H^2\rho^2 + W_{420M}H^4\rho^2$.

$$\begin{aligned} &W_{normalized\ third\ order\ plus\ fifth\ order\ field\ curvature} \\ &= W_{220ME}\left[\left(\vec{H}_{220ME}\cdot\vec{H}_{220ME}\right) + b_{220ME}\right](\vec{\rho}\cdot\vec{\rho}) \\ &+W_{420M}\left[\left(\vec{H}^2_{420M} + 2\vec{b}^2_{420M}\right)\cdot\vec{H}^2_{420M}\right](\vec{\rho}\cdot\vec{\rho}) \end{aligned} \quad (2)$$

Now, the aberration field behavior of field curvature is obtained from the vectorial wave aberration equation for asymmetric systems. It has one node that out of the field center under the assumption of third order aberration, and three colinear nodes will be generated when considering the influence of fifth order aberration. Then, the wave aberration of field curvature is transformed into longitudinal field curvature aberration for a more intuitive grasp of the best focal surface shape of off-axis systems. Because the longitudinal field curvature is defined as the deviation of the best focal surface from the Gaussian image plane, so it gives geometric expressions for the best focal surface shape. Here, the relationship between the wave aberration W and the transverse aberration $\vec{\Psi}$ as well as the geometric conversion between transverse aberration and longitudinal aberration δ are established in equation (3) for aberration

transformation. Where ∇W represents the gradient of wavefront, n' denotes the refractive index of the medium in image space, and R is the radius of the reference sphere in the exit pupil.

$$\begin{cases} \nabla W = \hat{i}\dfrac{\partial W}{\partial \rho_x} + \hat{j}\dfrac{\partial W}{\partial \rho_y} = -\dfrac{\vec{\Psi}\cdot n'}{R - W} \approx -\dfrac{\vec{\Psi}\cdot n'}{R} \\ \vec{\Psi} = \delta \cdot \sin u' = \delta \cdot \dfrac{\vec{\rho}}{R} \end{cases} \tag{3}$$

By substituting equation (1) and equation (2) into equation (3) respectively, we can obtain the longitudinal aberration of field curvature under the assumption of third-order aberration and the combined effect of low-order and high-order aberrations. Here, we assume that the off-axis system is symmetric about a certain plane, such as YOZ plane, given that most off-axis systems adopt this form. Therefore, the vectors $\vec{a}_{220M}$, $\vec{a}_{220ME}$, $\vec{a}_{420M}$ and $\vec{b}_{420M}$ associated with system tilt and decentration are all oriented at an angle of zero relative to the Hy-axis, and $i\vec{b}_{420M}$ is positioned at an angle of 90 with respect to $\vec{b}_{420M}$. For a clear understanding, the third order node and fifth order nodes in the tilted/decentered systems that are symmetric to YOZ plane are drawn in Fig. 1 (a). Now, the longitudinal aberration of field curvature can be written into scalar forms to provide the general representation of the optimal focal surface for off-axis systems. Equation (4) and equation (5) are the third-order longitudinal field curvature and the joint influence of the third-order and fifth-order on the longitudinal field curvature, where the parameter a_{220M}, a_{220ME}, a_{420M} and b_{420M} are the modules of the vectors $\vec{a}_{220M}$, $\vec{a}_{220ME}$, $\vec{a}_{420M}$ and $\vec{b}_{420M}$ respectively.

$$\delta_{\text{normalized third order field curvature}} = -\frac{2\cdot R^2}{n'}\cdot W_{220M}\left[x^2 + (y - a_{220M})^2 + b_{220M}\right] \tag{4}$$

$$\delta_{\text{normalized third order plus fifth order field curvature}} = -\frac{2\cdot R^2}{n'}\left\{\begin{array}{c} W_{220ME}\left[x^2 + (y - a_{220ME})^2 + b_{220ME}\right] \\ +W_{420M}\left[\left(x - \sqrt{2}\,b_{420M}\right)\left(x + \sqrt{2}\,b_{420M}\right) + (y - a_{420M})^2\right]\cdot\left[x^2 + (y - a_{420M})^2\right] \end{array}\right\} \tag{5}$$

Based on equation (4), it becomes evident that under the approximation of third-order aberration, the best focal surface of off-axis optical systems takes the shape of an off-axis paraboloid. This paraboloid is eccentric from the field center by a distance of a_{220M}, and it is also longitudinally shifted from the Gaussian image plane by a distance of $2R^2 W_{220M} b_{220M}$. According to the first term of equation (5), the vertex location and curvature of the off-axis paraboloid-shaped focal surface are altered due to the influence of the fifth-order aberration. Furthermore this new off-axis paraboloid also exhibits a certain degree of distortion due to the influence of quartic term, with the shape and magnitude of the distortion determined by the three nodes of the fifth order term $\vec{a}_{420M}$, $\vec{a}_{420M} \pm i\sqrt{2}\vec{b}_{420M}$ and wave aberration coefficient of fifth order field curvature W_{420M}. Therefore, under the influence of high order aberrations, the best focal surface becomes more complex and exhibits a freeform shape. This typically occurs in multimirror systems with large fields of view/aperture. Fig. 1(b) and (c) plot the contour maps of the best focal surface shape under third-order aberration alone and when considering the higher-order aberrations created by equation (4) and equation (5) respectively. Similarly, for the systems with rotational symmetry, the best focal surface is a paraboloid under third order assumption and an asphere when high order aberrations exist, because the parameters that are related to the component tilt/decenter is zero.

3. Off-axis three-mirror system design

In this section, an off-axis three-mirror system is used as an example to explore the advantages of combining freeform mirrors with a freeform sensor in reducing the system volume. For comparative analysis, off-axis three-mirror systems based on flat, spherical, and freeform image surfaces are designed separately under the same design parameters.

3.1. Design parameters

Here, we consider planetary science as a potential application and focus on flyby missions for solar system object exploration [35,36]. This implies that the system needs to cover a wide area of the object in a limited time and have a wide spectrum range to obtain information on different aspects of the object. Therefore, a fast, wide-field reflective optical system is preferred. In addition, such missions place high demands on the size and weight of the instrument, so we expect all three

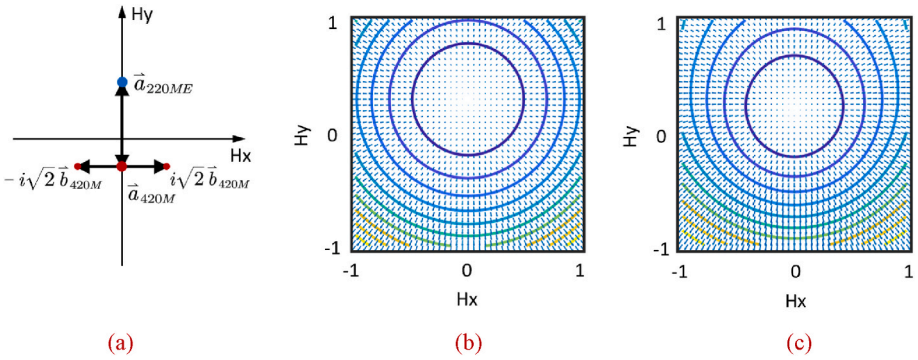

Fig. 1. Nodal orientation of field curvature aberration and optimal focal surface contour maps for tilted/decentered systems symmetrical to the YOZ plane. (a) The orientation of third-order node (blue) and fifth-order nodes (red); (b) Contour map of the off-axis parabolic focal surface created by equation (4); (c) Contour map of freeform focal surface created by equation (5).

Table 1
Design parameters of the off-axis three-mirror system.

Parameter	Value
Entrance pupil diameter	100 mm
F number	2.0
Field of view	12.4°(diagonal)
Reference wavelength	550 nm
Enclosed energy	≥90% per pixel
Distortion	≤2%

designs in this study to be optimized to their minimum volume while meeting the required imaging performance. The detailed design specifications are listed in Table 1, and the detector used is the GIGAPYX 4600 CMOS full-frame sensor (46 megapixels, 4.4 μm pitch). It should be noted here that these parameters were chosen based on previous flyby missions with enhanced field-of-view and F-number parameters and are therefore a good candidate for demonstration purpose.

3.2. Optical system design

In the work presented here, a set of Zernike fringe polynomials is employed to describe the freeform surfaces in the optical system. As Zernike polynomials have a direct connection to optical aberrations, they enable optical designers to conduct controlled optimization of the freeform surfaces with the help of aberration theory. This aids in limiting the overall freeform departure of a surface, ultimately reducing system sensitivity, fabrication costs, and testing difficulties. The sag, z, of a Zernike freeform surface is mathematically represented in equation (6), where c is the curvature of the base sphere, k is the conic constant, r is the radial coordinate of the surface, ρ is the normalized radial ray coordinate, and φ corresponds to the angular ray coordinate, N is the number of Zernike coefficients, A_i represents the coefficient of the ith Zernike Fringe polynomial Z_i.

$$z = \frac{cr^2}{1+\sqrt{1-(1+k)c^2r^2}} + \sum_{i=1}^{N} A_i Z_i(\rho,\varphi) \tag{6}$$

The "zigzag" geometry is adopted in this paper to design three off-axis systems based on different image surface shapes. The "zigzag" geometry, as proven by Bauer [6], is considered the optimal configuration for realizing freeform optical devices compared to other geometries. It enables the most performant and compact designs. Therefore, this structure ensures that all three systems achieve the desired imaging quality without being constrained by the design geometry while maintaining a smaller overall volume.

Firstly, the off-axis three-mirror system based on flat image surface is designed. In the initial optimization phase, the nodal aberration theory based on freeform surfaces [37] is employed to guide the design of the freeform mirror surfaces and to accelerate the convergence of the evaluation function. Specifically, when the ith Zernike coefficient is large and remains field constant, the coefficient A_i of the freeform surface at the stop or pupil is preferentially released as the optimization variable. If the ith Zenlike coefficient is field dependent, we release the coefficients A_i on freeform surfaces that are displaced longitudinally away from the stop or pupil in preference. Subsequently, other Zernike coefficients symmetric to the Y-axis are progressively released up to the 28th to meet the required imaging quality. Next, minimizing the system volume can be accomplished by a reduction in any of the three system dimensions without sacrificing imaging performance. The stepwise optimization is used in the design process to avoid getting trapped in shallow local minima. Additionally, the distortion requirements, first-order optical constraints and implicit flat-field conditions are needed to be met throughout the design process. Simultaneously, the distances between rays and mirrors, as well as between two adjacent mirrors are controlled to be greater than 10 mm to avoid obscuration and mirror interference.

When designing the off-axis three-mirror system based on spherical image surface, field curvature is compensated by the curved image surface. The initial curvature of the image surface is obtained by calculating the Petzval curvature, and in the subsequent optimization process, it is treated as a variable and automatically optimized by algorithm for the optimal image surface curvature of the system. Then, the volume of the system is continuously reduced to its minimum using the same method as for the design with flat image surface. In the freeform image surface-based design, we use the design of the spherical image surface as a starting point. In the process of minimizing the volume of this system, the astigmatism and coma terms are first added to the image surface to enhance the imaging performance. This is because the deviation of the off-axis paraboloid from its best-fit sphere is primarily composed of astigmatism and coma [38]. Afterwards other Zernike terms symmetric to the Y-axis are successively added up to 16th to perturb the shape of the image surface until the desired imaging quality is achieved. Care must be taken during this process to avoid excessive sag and slope in freeform image surface, which can lead to detector breakage failure during bending, and if necessary, a sum-of-squares penalty of the Zernike coefficients can be applied to constrain the slope of the surface [39].

Based on the design strategies outlined above, we obtain the design results after optimization for three different systems. Since the imaging quality of the three designs is comparable, only the imaging quality evaluation graphs for the design based on freeform image surface are present here. Fig. 2 shows the enclosed energy curves, modulation transfer function (MTF) curves, and distortion map respectively. The enclosed energy for all three designs is greater than 90% within one pixel. The MTF graph intuitively demonstrates the imaging capability of the systems, with all three designs achieving near diffraction limited imaging performance, which is consistent with the results of the enclosed energy plot because of the small pixel size of the selected detector. Additionally, the calculated maximum distortion based on the design with flat, spherical and freeform image surface are 1.7%, 1.6%, and 1.0% respectively, meeting the design requirements.

Fig. 3 illustrates the obtained minimum volume of the three systems while meeting required imaging performance. The minimum volume for the flat detector design is 49.97L. By directly compensating for field curvature aberration with spherical and freeform detectors, the volume of the off-axis three-mirror system is reduced to 19.85L and further to 9.86L, around five-fold reduction in volume. The results show that the curved detector, whether spherical or freeform shape, can highly compress the size and weight of the freeform off-axis three-mirror system, and the design based on freeform image surface shows a smaller system volume than the design based on spherical image surface. As stated in Section 2, the optimal focal surface shape for off-axis systems is complex and does not have rotational symmetry, so the freeform-shaped image surface can better compensate for this irregular field curvature aberration in off-axis systems.

To give a basic understanding of the surface complexity of the resulting optical surfaces in the three designs, the surface sag departure and slop departure of all the freeform mirrors after removing the best fit sphere (BFS) are shown in Table 2. The maximum peak-to-valley (PV) departure among all the mirrors in three designs is about 350 μm, and the maximum slope departure for all the mirrors not over 0.5°. Smaller sag and slope values represent that the freeform surfaces are much easier to be fabricated and tested.

From the off-axis three-mirror system design results, it is evident that spherical/freeform detectors can greatly reduce the size of freeform off-axis systems. Therefore, in situations where freeform mirrors are unable to meet the required volume specifications for a system, considering spherical/freeform detectors could be a viable solution to obtain the desired performance while achieving a more compact packaging volume.

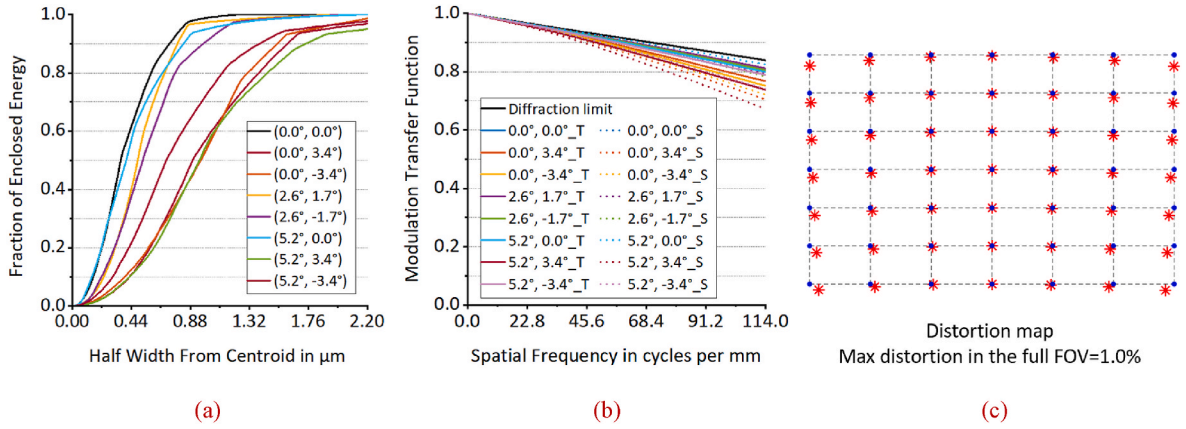

Fig. 2. Optical imaging quality evaluation graphs based on the design of freeform image surface. (a) The enclosed energy curves over the full field of view; (b) the modulation transfer function curves over the full field of view, in which the solid line represents the MTFs in meridional direction and the dashed line represents the MTFs in sagittal direction; (c) the distortion map calculated based on the curved image surface, in which the blue dots represent the ideal position of the image point and the red stars represent the real position of the image point, and the distortion shown in the map is scaled up by a factor of 5 for visualization.

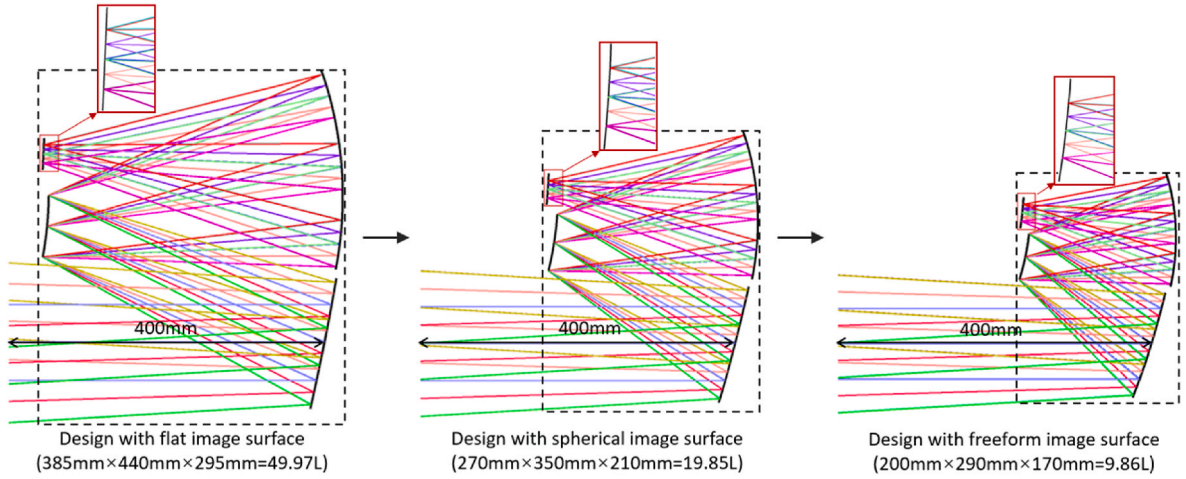

Fig. 3. Optical layout and volume parameters for three designs based on flat, spherical and freeform image surfaces, respectively. The distance between the ray starting point and the center of the first mirror is set to the same value (400 mm) for all three designs in order to highlight the dimensional differences among the three designs. The small area near the focal surface is magnified by a factor of 3 for all three designs to obtain a better visual effect.

Table 2
Mirror surface complexity of the three designs with flat, spherical and freeform image surface.

	PV Sag Departure (μm)			Max Slope Departure (°)		
	Flat sensor	Spherical sensor	Freeform sensor	Flat sensor	Spherical sensor	Freeform sensor
M1	76	59	123	0.09°	0.08°	0.20°
M2	174	69	67	0.42°	0.36°	0.23°
M3	354	163	140	0.30°	0.37°	0.45°

Table 3
Surface error tolerance results of mirrors and sensor for the design of freeform image surface.

	Curvature radius error		RMS surface figure error	
	ΔR	Δ Enclosed energy	RMS Surface irregularity	Δ Enclosed energy
M1	2 fringes	0.022	50 nm	0.022
M2	3 fringes	0.014	30 nm	0.080
M3	4 fringes	0.010	50 nm	0.040
Image surface	20 fringes	0.010	6 μm	0.012

3.3. Sensitivity analysis

Taking the design based on freeform image surface as an example, a root sum square (RSS) sensitivity analysis is performed on the mirror fabrication errors and the system assembly errors to evaluate the as-built performance of the design. The determination of tolerance values is based on the criterion that the closed energy across the full field of view is greater than 90% within two pixels. In the RSS sensitivity analysis, the system is individually perturbed with each tolerance. The resulting performance drop is calculated after applying a detector refocus as a default compensator. The RSS of all performance drops is taken and subsequently added to the nominal performance of the system to yield the predicted as-built performance.

The assembly tolerances used here consist of mirrors and detector tip/tilt of ±0.17 mrad, clocking of ±0.3 mrad, X/Y decenters of ±0.02 mm and air thickness of ±0.05 mm. The compensator refocus is within ±0.06 mm. There is a huge difference between the surface error of freeform mirrors and curved freeform detector, which are detailly listed in Table 3. The curvature radius errors of the three optical mirrors must meet the accuracy of at least 4 fringes, while the curvature radius tolerance of the detector is only 20 fringes at the testing wavelength of 632.8 nm. The required root-mean-square (RMS) surface figure error for optical mirrors is at least 50 nm, but for detector 6 μm RMS surface figure error is enough. It is found that the required surface precision for freeform detectors is quite lower than that for freeform optical mirrors, differing by at least two orders of magnitude. This is because the surface tolerance of the image surface is determined by the allowable defocus of the system, but the surface error of the optical mirror will cause drastic changes in various aberrations. The tolerance values presented here are feasible according to current high-precision manufacturing techniques, and the tolerance values can be further loosened by adding one more compensator in the system, like mirror or detector tip/tilt.

4. Manufacturability of the freeform detector

A standard COMS sensor consists of a silicon die glued on a ceramic package. Wire bonding from the die to the package surface provides the electrical connections. Finally, a glass window protects the sensor surface from mechanical or environmental solicitations. For a curved sensor, several changes are required to adapt this standard structure. First, the sensor is thinned with a grinding equipment to make the sensor mechanically "flexible", then they are glued onto a curved substrate. The required shape of the CMOS is, hence, due to the shape of the substrate. The sensors are then wire bonded keeping the packaging identical to the standard flat sensor [25].

In the manufacturing process of curved detectors, the bendability of the silicon die is a primary and critical issue, it determines whether the detector will fail or survive when curved into a certain shape to a large extent. To ensure that the silicon die does not break when bending into the required freeform shape during curving process, the finite element simulation is needed to analyze the mechanical behavior of the curved silicon die. Here we present the two kinds of breakage limits generally used in the sensor curving process according to different die pretreatment [40,41]. The first criterion ($\sigma 1_{max1}$ <200 MPa) is the breakage limit with standard grinding and dicing. The second criterion ($\sigma 1_{max2}$ <500 MPa) is the breakage limit with an advanced grinding process and die preparation. We chose 200 MPa mechanical limit as the criterion for evaluating the bending capability of freeform curved sensor in this paper.

According to the theory of plates and shells [42], the stress of the curved silicon die depends on its geometrical parameters: size, thickness and curvature. The detector mechanical dimension is 40.36mm × 41.22 mm and it is thinned to 150 μm before curving to ensure its elasticity. Therefore, the successful preparation of the final detector depends on the shape into which it is bent. To answer this question, a 2D shell model is created firstly with a free edge boundary condition applied at the die center $(\rho, \theta, z) = (0, 0, 0)$ to prevent rigid-body motion during simulation. Then, the freeform shape is generated by applying a vertical displacement $z = f(\rho, \theta)$ to the silicon die. After performing the nonlinear analysis on the 2D shell elements, we obtain the stress distribution of the silicon die when bent into the freeform shape.

After removing base sphere, the freeform image surface is mainly composed of primary astigmatism terms, primary coma terms, and secondary coma terms. These Zernike terms eventually distort the image

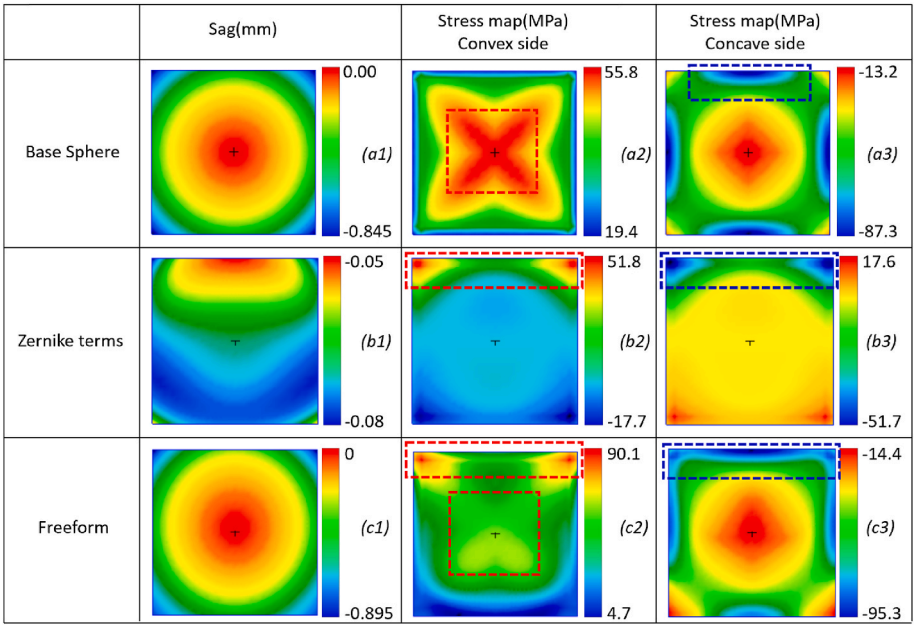

Fig. 4. Sag maps and stress distribution maps for silicon dies bent into three different shapes: a spherical shape, a shape containing only Zernike terms, and a freeform shape. The freeform shape is formed by the superposition of the base sphere and Zernike terms. First column (*a1, b1, c1*): Sag maps of the silicon dies. Second column (*a2, b2, c2*): Stress distribution maps on the convex side of the silicon dies. Third column (*a3, b3, c3*): Stress distribution map on the concave side of the silicon dies.

surface into an irregular surface. The base sphere, Zernike terms and the final freeform shape are shown in Fig. 4(a1), (b1) and (c1) respectively. The freeform image surface has a certain degree of eccentricity, and the contour of the surface is not a circle due to the influence of high-order field curvature.

Fig. 4 shows the stress distribution when the silicon chip is bent into a base spherical surface, a Zernike surface, and a freeform surface composed of the two. It can be found that there is a certain degree of similarity in the mechanical behavior of the silicon chip that is bent into spherical shape and freeform shape. Although the image surface is not a perfect sphere, it still maintains obvious unidirectional curvature characteristics, that is, the sign of the curvature value on one side of the monolithic silicon is always the same and has no curvature reversal. Therefore, the convex side is under tension everywhere (the stress value is positive) and the concave side is under compression everywhere (the stress value is negative). However, the stress distribution in the bending state of the freeform shape is not symmetrical. Its stress distribution is the superposition of spherical bending and Zernike bending. As shown in the red dashed box in Fig. 4(c2), the areas with higher stress values on the silicon die are at the center and the upper two corners, which correspond to the areas where the maximum stress is located in Fig. 4 (a1) and (b1) respectively. The same is true for the blue dashed box in Fig. 4(c3). In addition, it can be seen from the stress distribution in the Zernike bending state that even though the sag introduced by Zernike terms is much smaller than that of the base sphere, its stress value is equivalent to that of the base sphere. Therefore, large sag departure or slope departure should be avoided in the design of freeform image surface, because this may cause large local stresses, which will eventually lead to fracture failure of the detector when bending.

The finite element analysis results indicate that the detector can be successfully bent into the freeform shape designed in this paper without experiencing breakage. Furthermore, considering the experimental measurements of spherical sensors available in our laboratory [27], where curvature radii can reach ±0.1 mm and RMS surface irregularity can achieve 1 μm, it is evident that the tolerance of the designed freeform sensor in this study is achievable based on the results of Table 3, and this will be validated once the freeform sensor is manufactured and tested.

5. Discussion

In this section, we discuss the impact of the proposed design concept on the parameter space of imaging instruments in the field of planetary exploration. Fig. 5 lists some of the optical performance parameters and volume parameters of imaging instruments that have been used for missions exploring solar system objects in recent decades. The horizontal axis represents the angular resolution of the instrument, the vertical axis represents the field of view, the size of the circle represents the relative aperture, and the color of the circle represents the volume of the system. Additionally, 'M' indicates that the instrument is a reflective structure consisting of mirrors, 'L' indicates a refractive system consisting of lenses, and 'ML' indicates a catadioptric structure. In the figure, our off-axis three-mirror system based on the proposed design concept is marked with a red asterisk for comparative analysis. It should be noted here that the discussion primarily focuses on flyby and orbiter missions, excluding considerations for landers and rovers. Consequently, the instruments listed in the figure typically cover a broad spectral range, spanning from UV–visible to near-infrared bands, and most of them feature reflective structures. Next, we compare and analyze these instruments in terms of volume, relative aperture, field of view and resolution, respectively.

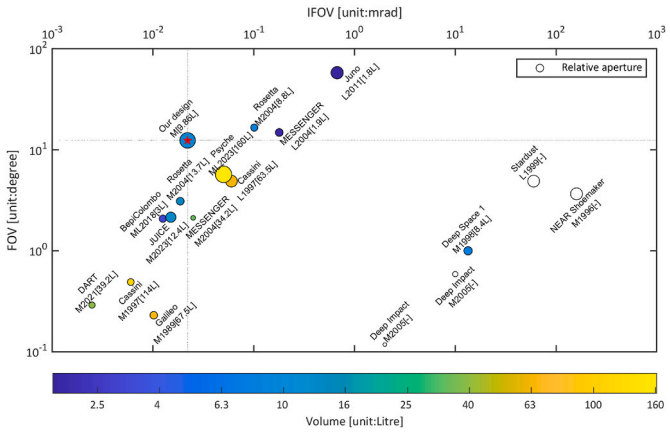

Fig. 5. Scatterplot of the parameters of optical imaging instruments in the field of planetary exploration in recent decades [35,36,43–46] and the parameters of our design in this paper (marked by red asterisks). Horizontal axis: Resolution; Vertical axis: Field of view; Circle size: Relative aperture; Circle color: System volume (optical system only); M: reflective structures; L: refractive structure; ML: catadioptric structure; Launch year follows structure label. Volume values are shown in brackets, with unknown volumes unfilled with colors.

In terms of volume, these instruments are generally relatively small, with more than half of them being less than 15 L in size. The smallest volumes can be found in refractive systems (labelled L), which have a large field of view but low resolution. The opposite is true for reflective configurations, which typically have high resolution but small fields of view and relatively large volumes. Comparing M2004 and L2004 [43], it can be seen that the reflective system has to sacrifice size in order to achieve the similar field of view. In addition, the resolution of M2004 is not high because the field of view and the resolution of the instrument are usually limited by the system size and optical aberrations and thus cannot be satisfied at the same time. In contrast, our design achieves higher resolution at approximately the same field of view with a larger relative aperture while keeping the volume relatively small, whereas the freeform three-mirror system design based on a flat detector requires a much larger volume (~50L).

Regarding relative aperture, higher values are also achieved at the expense of volume, as in the case of the ML2023 [44] and L1997 [45]. But the design in this paper not only achieves a relative aperture similar to that of the ML2023, but also has a larger field of view and higher resolution, and notably, a smaller volume.

In terms of field of view and resolution, it is found that some of the earlier instruments in this field have relatively poor optical performance due to the limitations of the technology level at that time. However, as the technology has evolved, the imaging performance of the instruments has climbed and is gradually approaching the upper left corner of the figure, i.e., large field of view and high resolution. But it is obvious that the parameters of these instruments are stopped by an invisible boundary and cannot advance further. The design presented in this paper can further break through this limitation and achieve better imaging performance with relatively small size and large relative aperture.

Through the above analyses, it can be concluded that the proposed design concept in this paper can improve the performance of the system while maintaining a relatively small volume, and thus can broaden the parameter space of the instruments in this field to a certain extent. So it will provide a feasible solution to achieve higher imaging performance for future planetary exploration missions.

6. Conclusion

To further enhance the compactness of off-axis reflective optical imaging systems, this paper introduces an innovative approach by combining freeform mirrors with a freeform detector in the design of off-axis systems. Firstly, nodal aberration theory is adopted to analyze and demonstrate that the optimal focal surface shape for off-axis systems is a freeform surface rather than a perfect sphere. Secondly, an off-axis three-mirror system is taken as an example to show the advantages of the proposed design in reducing the volume of off-axis systems. The

three systems based on flat, spherical, and freeform detectors are respectively designed under the same imaging parameters: a 100 mm aperture at F/2 and a 12.4-degree diagonal field of view. The design results indicate an 80% reduction in system volume with the use of freeform detector compared to the flat detector design. This ultimately allows the off-axis three-mirror system to achieve near-diffraction-limited imaging quality within a compact 10L volume. Thirdly, the mechanical behavior of the curved silicon chip is analyzed through finite element simulation, ensuring that the silicon chip can be smoothly bent into the designed freeform shape without facing fracture failures. Furthermore, the surface precision required for the freeform detector is at least two orders of magnitude lower than that for the freeform mirrors, and which is achievable given the current level of curved detector manufacturing. This will be further proved once the freeform detector is fabricated and tested in the laboratory. Finally, we show the ability of the proposed design concept to expand the parameter space of scientific imaging instruments in the field of planetary science. This concept can achieve higher performance imaging systems within relatively small volumes, thus offering feasible solutions for future planetary exploration missions. In addition, it can also be applied in other space science fields such as Earth observation, space weather monitoring, astronomical telescopes, and more. We anticipate that the presented design concept will open up more possibilities for the design of demanding off-axis optical systems.

CRediT authorship contribution statement

Jiawei Liu: Writing – original draft, Methodology, Formal analysis, Conceptualization. **Emmanuel Hugot:** Writing – review & editing, Validation, Supervision, Resources. **Eduard Muslimov:** Writing – review & editing, Validation. **Simona Lombardo:** Writing – review & editing.

Declaration of competing interest

The authors declare that they have no known competing financial interests or personal relationships that could have appeared to influence the work reported in this paper.

Data availability

Data will be made available on request.

Acknowledgments

J. LIU thanks for the support of China Scholarship Council (CSC).

References

[1] Z. Qu, X. Zhong, K. Zhang, Y. Wang, L. Li, J. Liu, C. Zeng, Automatic compact-volume design strategy for unobscured reflective optical systems based on conicoid surfaces, Opt Commun. 533 (2023) 129304.
[2] P.A. Lightsey, C.B. Atkinson, M.C. Clampin, L.D. Feinberg, James Webb Space Telescope: large deployable cryogenic telescope in space, Opt. Eng. 51 (2012) 011003.
[3] Y. Liu, A. Bauer, T. Viard, J.P. Rolland, Freeform hyperspectral imager design in a CubeSat format, Opt Express 29 (2021) 35915–35928.
[4] M. Strojnik, B. Bravo-Medina, A. Beltran-Gonzalez, Y. Wang, Off-Axis three-mirror optical system designs: from cooke's triplet to remote sensing and surveying instruments, Appl. Sci. 13 (2023) 8866.
[5] X. Yan, Y. Li, L. Liu, K. Liu, Grouping design method dependence on an illumination system and large off-axis distance for an anamorphic extreme ultraviolet lithography objective, Appl. Opt. 61 (2022) 806–811.
[6] A. Bauer, E.M. Schiesser, J.P. Rolland, Starting geometry creation and design method for freeform optics, Nat. Commun. 9 (2018) 1756.
[7] K. Dohlen, M. Saisse, G. Claeysen, P.L. Lamy, J.-L. Boit, Optical designs for the Rosetta narrow-angle camera, Opt. Eng. 35 (1996) 1150–1157.
[8] J.P. Rolland, M.A. Davies, T.J. Suleski, C. Evans, A. Bauer, J.C. Lambropoulos, K. Falaggis, Freeform optics for imaging, Optica 8 (2021) 161–176.
[9] K. Fuerschbach, J.P. Rolland, K.P. Thompson, A new family of optical systems employing φ-polynomial surfaces, Opt Express 19 (2011) 21919–21928.
[10] W. Wu, G. Jin, J. Zhu, Optical design of the freeform reflective imaging system with wide rectangular FOV and low F-number, Results Phys. 15 (2019) 102688.
[11] J. Reimers, A. Bauer, K.P. Thompson, J.P. Rolland, Freeform spectrometer enabling increased compactness, Light Sci. Appl. 6 (2017) e17026.
[12] A. Rakich, N. Rumsey, Method for deriving the complete solution set for three-mirror anastigmatic telescopes with two spherical mirrors, J. Opt. Soc. Am. A, JOSAA 19 (2002) 1398–1405.
[13] A. Bauer, J.P. Rolland, Roadmap for the unobscured three-mirror freeform design space, Opt Express 29 (2021) 26736–26744.
[14] H.C. Ko, M.P. Stoykovich, J. Song, V. Malyarchuk, W.M. Choi, C.-J. Yu, J. B. Geddes III, J. Xiao, S. Wang, Y. Huang, J.A. Rogers, A hemispherical electronic eye camera based on compressible silicon optoelectronics, Nature 454 (2008) 748–753.
[15] S.B. Rim, P.B. Catrysse, R. Dinyari, K. Huang, P. Peumans, The optical advantages of curved focal plane arrays, Opt Express 16 (2008) 4965–4971.
[16] R. Dinyari, S.-B. Rim, K. Huang, P.B. Catrysse, P. Peumans, Curving monolithic silicon for nonplanar focal plane array applications, Appl. Phys. Lett. 92 (2008) 091114.
[17] O. Iwert, B. Delabre, The challenge of highly curved monolithic imaging detectors, in: High Energy, Optical, and Infrared Detectors for Astronomy IV, SPIE, 2010, pp. 646–654.
[18] O. Iwert, D. Ouellette, M. Lesser, B. Delabre, First results from a novel curving process for large area scientific imagers, in: High Energy, Optical, and Infrared Detectors for Astronomy V, SPIE, 2012, pp. 581–594.
[19] D. Dumas, M. Fendler, N. Baier, J. Primot, E. le Coarer, Curved focal plane detector array for wide field cameras, Appl. Opt. 51 (2012) 5419–5424.
[20] D. Dumas, M. Fendler, F. Berger, B. Cloix, C. Pornin, N. Baier, G. Druart, J. Primot, E. le Coarer, Infrared camera based on a curved retina, Opt. Lett. 37 (2012) 653–655.
[21] E. Hugot, W. Jahn, B. Chambion, L. Nikitushkina, C. Gaschet, D. Henry, S. Getin, G. Moulin, M. Ferrari, Y. Gaeremynck, Flexible focal plane arrays for UVOIR wide field instrumentation, in: High Energy, Optical, and Infrared Detectors for Astronomy VII, SPIE, 2016, pp. 514–522.
[22] B. Chambion, C. Gaschet, T. Behaghel, A. Vandeneynde, S. Caplet, S. Gétin, D. Henry, E. Hugot, W. Jahn, S. Lombardo, M. Ferrari, Curved sensors for compact high-resolution wide-field designs: prototype demonstration and optical characterization, in: Photonic Instrumentation Engineering V, SPIE, 2018, pp. 240–249.
[23] K. Itonaga, T. Arimura, K. Matsumoto, G. Kondo, K. Terahata, S. Makimoto, M. Baba, Y. Honda, S. Bori, T. Kai, K. Kasahara, M. Nagano, M. Kimura, Y. Kinoshita, E. Kishida, T. Baba, S. Baba, Y. Nomura, N. Tanabe, N. Kimizuka, Y. Matoba, T. Takachi, E. Takagi, T. Haruta, N. Ikebe, K. Matsuda, T. Niimi, T. Ezaki, T. Hirayama, A novel curved CMOS image sensor integrated with imaging system, in: 2014 Symposium on VLSI Technology (VLSI-Technology): Digest of Technical Papers, 2014, pp. 1–2.
[24] B. Guenter, N. Joshi, R. Stoakley, A. Keefe, K. Geary, R. Freeman, J. Hundley, P. Patterson, D. Hammon, G. Herrera, E. Sherman, A. Nowak, R. Schubert, P. Brewer, L. Yang, R. Mott, G. McKnight, Highly curved image sensors: a practical approach for improved optical performance, Opt Express 25 (2017) 13010–13023.
[25] S. Lombardo, T. Behaghel, B. Chambion, S. Caplet, W. Jahn, E. Hugot, E. Muslimov, M. Roulet, M. Ferrari, C. Gaschet, D. Henry, Curved detectors for astronomical applications: characterization results on different samples, Appl. Opt. 58 (2019) 2174–2182.
[26] E. Muslimov, D. Valls-Gabaud, G. Lemaître, E. Hugot, W. Jahn, S. Lombardo, X. Wang, P. Vola, M. Ferrari, Fast, wide-field and distortion-free telescope with curved detectors for surveys at ultralow surface brightness, Appl. Opt. 56 (2017) 8639–8647.
[27] S. Lombardo, E. Muslimov, G. Lemaître, E. Hugot, Next-generation telescopes with curved focal surface for ultralow surface brightness surveys, Mon. Not. R. Astron. Soc. 488 (2019) 5057–5064.
[28] K. Joaquina, Curved Sensors for Ultraviolet Aurora Monitoring from Space, 2021. PhD These, Aix-Marseille.
[29] I. Racicot, E. Muslimov, S. Chemla, K. Blaize, M. Ferrari, F. Chavane, High resolution, wide field optical imaging of macaque visual cortex with a curved detector, J. Neural. Eng. 19 (2022) 066022.
[30] C. Gaschet, W. Jahn, B. Chambion, E. Hugot, T. Behaghel, S. Lombardo, S. Lemared, M. Ferrari, S. Caplet, S. Gétin, A. Vandeneynde, D. Henry, Methodology to design optical systems with curved sensors, Appl. Opt. 58 (2019) 973–978.
[31] K. Thompson, Description of the third-order optical aberrations of near-circular pupil optical systems without symmetry, J. Opt. Soc. Am. A 26 (2009) 699, 699.
[32] E. Muslimov, E. Hugot, W. Jahn, S. Vives, M. Ferrari, B. Chambion, D. Henry, C. Gaschet, Combining freeform optics and curved detectors for wide field imaging: a polynomial approach over squared aperture, Opt Express 25 (2017) 14598–14610.
[33] E. Muslimov, E. Hugot, M. Ferrari, T. Behaghel, G.R. Lemaitre, M. Roulet, S. Lombardo, Design of optical systems with toroidal curved detectors, Opt. Lett. 43 (2018) 3092–3095.
[34] K.P. Thompson, Multinodal fifth-order optical aberrations of optical systems without rotational symmetry: the astigmatic aberrations, J. Opt. Soc. Am. A 28 (2011) 821–836.
[35] O. Grasset, M.K. Dougherty, A. Coustenis, E.J. Bunce, C. Erd, D. Titov, M. Blanc, A. Coates, P. Drossart, L.N. Fletcher, H. Hussmann, R. Jaumann, N. Krupp, J.-P. Lebreton, O. Prieto-Ballesteros, P. Tortora, F. Tosi, T. Van Hoolst, JUpiter ICy moons Explorer (JUICE): an ESA mission to orbit Ganymede and to characterise the Jupiter system, Planet. Space Sci. 78 (2013) 1–21.

[36] J. Benkhoff, G. Murakami, W. Baumjohann, S. Besse, E. Bunce, M. Casale, G. Cremosese, K.-H. Glassmeier, H. Hayakawa, D. Heyner, H. Hiesinger, J. Huovelin, H. Hussmann, V. Iafolla, L. Iess, Y. Kasaba, M. Kobayashi, A. Milillo, I. G. Mitrofanov, E. Montagnon, M. Novara, S. Orsini, E. Quemerais, U. Reininghaus, Y. Saito, F. Santoli, D. Stramaccioni, O. Sutherland, N. Thomas, I. Yoshikawa, J. Zender, BepiColombo - mission overview and science goals, Space Sci. Rev. 217 (2021) 90.

[37] K. Fuerschbach, J.P. Rolland, K.P. Thompson, Theory of aberration fields for general optical systems with freeform surfaces, Opt Express 22 (2014) 26585–26606.

[38] J. Lubliner, J.E. Nelson, Stressed mirror polishing. 1: a technique for producing nonaxisymmetric mirrors, Appl. Opt. 19 (1980) 2332–2340.

[39] N. Takaki, A. Bauer, J.P. Rolland, On-the-fly surface manufacturability constraints for freeform optical design enabled by orthogonal polynomials, Opt Express 27 (2019) 6129–6146.

[40] M.Y. Tsai, C.H. Chen, Evaluation of test methods for silicon die strength, Microelectron. Reliab. 48 (2008) 933–941.

[41] J.H. Zhao, J. Tellkamp, V. Gupta, D.R. Edwards, Experimental evaluations of the strength of silicon die by 3-point-bend versus ball-on-ring tests, IEEE Trans. Electron. Packag. Manuf. 32 (2009) 248–255.

[42] S. Timoshenko, Theory of Plates and Shells, second ed., McGraw-Hill, New York, 1959.

[43] S.C. Solomon, R.L. McNutt, R.E. Gold, M.H. Acuña, D.N. Baker, W.V. Boynton, C. R. Chapman, A.F. Cheng, G. Gloeckler, J.W. Head III, S.M. Krimigis, W. E. McClintock, S.L. Murchie, S.J. Peale, R.J. Phillips, M.S. Robinson, J.A. Slavin, D. E. Smith, R.G. Strom, J.I. Trombka, M.T. Zuber, The MESSENGER mission to Mercury: scientific objectives and implementation, Planet. Space Sci. 49 (2001) 1445–1465.

[44] W. Hart, G.M. Brown, S.M. Collins, M. De Soria-Santacruz Pich, P. Fieseler, D. Goebel, D. Marsh, D.Y. Oh, S. Snyder, N. Warner, G. Whiffen, L.T. Elkins-Tanton, J.F. Bell, D.J. Lawrence, P. Lord, Z. Pirkl, Overview of the spacecraft design for the Psyche mission concept, in: 2018 IEEE Aerospace Conference, IEEE, Big Sky, MT, 2018, pp. 1–20.

[45] C.L. Kahn, W.S. King, Cassini imaging science subsystem, in: Cassini/Huygens: A Mission to the Saturnian Systems, SPIE, 1996, pp. 187–196.

[46] Science Missions, (n.d.). https://science.nasa.gov/science-missions/(accessed April 6, 2024).